Pergamon

Int. J. Heat Mass Transfer. Vol. 39, No. 8, pp. 1665–1675, 1996
Copyright © 1996 Elsevier Science Ltd
Printed in Great Britain. All rights reserved
0017-9310/96 $15.00+0.00

0017-9310(95)00255-3

Numerical modeling of materials processing in microwave furnaces

J. CLEMENS and C. SALTIEL†
SCRAM Technology Inc., Glenmont, NY 12077, U.S.A.

(*Received* 13 *March* 1995 *and in final form* 27 *June* 1995)

Abstract—A detailed numerical model is presented for predicting electromagnetic fields in microwave waveguides and cavities, and the power deposition and temperature distribution in processed samples. Implementation of explicit finite difference schemes for solving the coupled unsteady Maxwell and energy equations is discussed. Simulations are performed illustrating the influence of working frequency, sample size and dielectric properties. The occurrence of resonant conditions, where constructive electromagnetic wave interference patterns produce high electric field intensities at discrete locations throughout the cavity, is shown to be the key ingredient for achieving high heating levels. The presence of coupled nonlinear processes is significant in materials which exhibit temperature dependent electromagnetic properties. This is illustrated in the processing of alumina, where local heating produces an exponential rise in temperature, once a critical temperature level is achieved.

1. INTRODUCTION

The ability of microwave radiation to penetrate and couple with materials has led to its extensive use in the food industry. More recently, microwaves are being considered for a wide variety of other uses. Compared to conventional heating methods, microwave processing can provide more rapid and uniform heating in a clean environment, offering improvements in product quality, the production of unique microstructures and properties, and reductions in manufacturing costs and processing times. Uniform heating reduces thermal stresses, avoiding cracking during processing. Selective heating is also possible since microwave absorption varies with material composition and structure. Industrial heating (large volume drying of textiles, ceramics and rubber) and materials development (polymer matrix composites and epoxy curing, ceramic sintering and binder burnout, and plasma processing) stand out as important microwave processing applications that have been studied [1–3]. Microwave processing can also be used to efficiently remove volatile constituents deep within materials. For example, sulfur can be removed from coal as a pre-combustion treatment [4], contaminants (such as petroleum derived hydrocarbons) removed from soils or sludges [5], and polymeric binders removed from ceramics during forming [6]. A new and exciting area for microwave heating applications is in the processing of hazardous wastes, finding use in the treatment of nuclear waste, gaseous air pollutants, sewage sludges and waste water, and contaminated soils [7].

The intensity and spatial distribution of microwave energy throughout a material specimen is dictated by the complexity of electromagnetic scattering and absorption within the material, as well as reflections at the enclosure walls. As a result, obtaining desired heating patterns or precise control of specimen temperature distribution is often problematic. To illustrate the complex nature of microwave processing devices, a cross-sectional view of some important processing components of a microwave oven is shown in Fig. 1. Microwave appliances have three major components: a microwave generator, a waveguide, and an applicator. In most commercial and industrial ovens, microwaves are generated by magnetron tubes. Once microwaves are produced they are fed into the applicator (cavity) through a transmission device called a waveguide. Waveguides and cavities come in a variety of shapes and sizes, which should be chosen for a specific application. Their design is generally dependent on operating frequency, the nature and dimensions of the product to be processed, and the type of processing (batch or continuous). While microwave hardware design has focused on electrical parameters governing wave propagation and attenuation, it is the thermal characteristics that ultimately determine the end-product and which need to be closely tied to the design process.

Cavities are broadly classified as either single-mode or multi-mode. Single-mode cavities support a single resonant mode at a given frequency, making the field distribution throughout the cavity very nonuniform. As a result, hot spots can occur in regions of high

---

† Author to whom correspondence should be addressed.

NOMENCLATURE

$\mathbf{B}$	magnetic induction [(N s) (C m)$^{-1}$]
C	specific heat [(W s) (kg °C)$^{-1}$]
c	speed of light [m s^{-1}]
$\mathbf{E}$	electric field intensity [V m^{-1}]
F	radiative view factor
f	frequency [Hz]
$\mathbf{H}$	magnetic field intensity [A m^{-1}]
h_f	convective heat transfer coefficient [W m^{-2} °C^{-1}]
k	thermal conductivity [W m^{-1} °C^{-1}] imaginary component of refractive index
n	real component of refractive index
Q_{em}	electromagnetic heat source [W m^{-3}]
Q_{total}	total average power absorbed per unit depth [W m^{-1}]
q_{conv}	convective heat loss [W m^{-2}]
q_{rad}	radiative heat loss [W m^{-2}]
T	temperature [°C].

Greek symbols

δ	skin depth [m]
ε	electric permittivity [C^2 (N m^2)$^{-1}$] radiative emissivity
λ	wavelength [m]
μ	magnetic permeability [(N s^2) C^{-2}]
ρ	density [kg m^{-3}]
σ	Stefan Boltzman constant [5.607×10^{-8} W m^{-2} K^4]
σ_e	electrical conductivity [S m^{-1}]
ω	angular frequency ($2\pi f$) [Hz].

Subscripts

a	ambient
e	edge
0	vacuum property
r	relative (property in medium/property in vacuum)
rms	root-mean-square.

Superscripts

n	discretized time step.

electric field intensity, requiring careful sizing and placement of materials. Single-mode cavities have been used successfully for processing small samples (typically less than 1.5 in in diameter) and fibers, but are generally not appropriate for larger specimen volumes. Multi-mode cavities attempt to avoid this problem by over-sizing the cavity and/or increasing the frequency of the excitation source so that a number of high-order modes are supported simultaneously. While the fields within an empty cavity will be more uniform, the electromagnetic field intensity can be highly distorted if an absorbing material is placed in the cavity. Field distortion for high loss materials, such as ceramics, will generally be much greater than for low loss materials, e.g. polymers. Achieving uniform temperatures within the processed sample will be difficult unless the electromagnetic field distribution can be well characterized and appropriate control measures taken, i.e. source pulsing, external surface heating, or simply moving the sample.

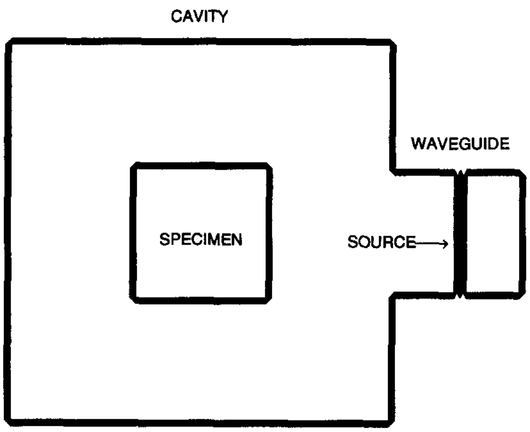

Fig. 1. Schematic diagram of microwave cavity, waveguide, specimen and radiation source.

In situations where materials absorb microwave radiation more efficiently at higher temperatures due to dramatic increases in electrical conductivity, a local exponential rise in temperature can occur. This phenomena, commonly referred to as *thermal runaway*, has been displayed in a variety of materials, including zirconia [8], alumina [9], macor (a machineable glass ceramic) [10], nickel zinc ferrite [11] and nylon [12]. Poor product quality and sample cracking are often exhibited if temperature levels and distributions cannot be controlled. Understanding, predicting, and preventing or controlling thermal runaway presents a major challenge to the development of microwave processing. A number of strategies have been employed to avoid thermal runaway, including hybrid heating (conventional plus microwave heat sources) [9] and various control techniques (e.g. PID [10]). Since the real challenge of controlling thermal runaway is to avoid local hot spots, a detailed knowledge of local electromagnetic field intensities is imperative. Some work has been performed to characterize thermal runaway via numerical modeling [9, 13–15]. While these efforts have included temperature dependent properties, none have accounted for the spatial variation in the electric field intensity within the processed sample.

While lumped and uniform energy deposition models are useful for understanding the qualitative influence of processing parameters, models which include the temporal and spatial variation of the electromagnetic field intensity within a cavity will provide a much more accurate means for predicting and assessing heating patterns. High quality predicative methods offer an inexpensive method to better assess the effects of sample size, shape, and physical properties with respect to cavity geometries, power inputs and working frequencies. A variety of numerical approaches are available to simulate microwave-material interactions [16]. Generally, simulation of microwave deposition requires the solution of the equations governing electromagnetic propagation, i.e. Maxwell's equations, within both the microwave cavity/waveguide and the processed material. The finite-difference time-domain (FDTD) method [17, 18] has been used to provide a full description of electromagnetic scattering and absorption and gives detailed spatial and temporal information of wave propagation. The method has received increased attention recently due to its versatility in handling complex shaped objects, a wide range of frequencies and stimuli, and a variety of materials, including those which exhibit frequency and temperature dependence. Time domain modeling is also useful for depicting resonant behavior [19], an important consideration in microwave processing. A discussion of the trade-offs between the FDTD method and other widely used methods for simulating electromagnetic-material interactions, e.g. spherical wave expansions and integral operators, can be found in refs. [19, 20]. References [21–23] specifically discuss FDTD methods applied directly to microwave heating of samples with constant and uniform electromagnetic and thermal properties.

To understand the influence of electromagnetic field patterns on microwave heating, we have developed a finite-difference time-domain model, coupled to a transient finite difference model for thermal transport. The FDTD expressions, as derived from Maxwell's equations, are presented along with discussions concerning numerical implementation as applied to microwave cavities. Two-dimensional waveguide/cavity simulations are performed illustrating the field distortion caused by the presence of a glossy material. We show that via slight variation of an operating parameter (the frequency), the local electrical intensity in an empty cavity can change significantly, simulating resonant and off-resonant conditions. Parametric studies of sample size and dielectric properties show the variations in power deposition for different specimen types. Numerical coupling between the electro-magnetic and thermal fields is described, and its significance is illustrated in the heating of alumina, which exhibits strong electromagnetic property temperature dependence. This simulation displays the local exponential temperature rise typical of thermal runaway.

2. ELECTROMAGNETIC FIELD EQUATIONS AND FDTD DISCRETIZATION

Characterization of the energy deposition and physical changes taking place in material properties during microwave processing requires solution of the electromagnetic and energy transport equations. The basic equations governing the electric and magnetic field vectors are expressed as the Maxwell curl relations [24]. These equations can be expressed in vector differential form in terms of the electric $\mathbf{E}$ (V m^{-1}) and magnetic $\mathbf{H}$ (A m^{-1}) fields as

$$\varepsilon\frac{\partial \mathbf{E}}{\partial t} = \nabla\times\mathbf{H}-\sigma_e\mathbf{E} \tag{1}$$

$$\mu\frac{\partial \mathbf{H}}{\partial t} = -\nabla\times\mathbf{E}, \tag{2}$$

where σ_e is the electrical conductivity, μ is the magnetic permeability and ε is the electrical permittivity. In rectangular coordinates, the curl equations can be expressed as a set of six coupled scalar partial differential equations

$$\varepsilon\frac{\partial \mathbf{E}_x}{\partial t} = \frac{\partial \mathbf{H}_z}{\partial y}-\frac{\partial \mathbf{H}_y}{\partial z}-\sigma_e\mathbf{E}_x \tag{3}$$

$$\varepsilon\frac{\partial \mathbf{E}_y}{\partial t} = \frac{\partial \mathbf{H}_x}{\partial z}-\frac{\partial \mathbf{H}_z}{\partial x}-\sigma_e\mathbf{E}_y \tag{4}$$

$$\varepsilon\frac{\partial \mathbf{E}_z}{\partial t} = \frac{\partial \mathbf{H}_y}{\partial x}-\frac{\partial \mathbf{H}_x}{\partial y}-\sigma_e\mathbf{E}_z \tag{5}$$

$$\mu\frac{\partial \mathbf{H}_x}{\partial t} = \frac{\partial \mathbf{E}_y}{\partial z}-\frac{\partial \mathbf{E}_z}{\partial y} \tag{6}$$

$$\mu\frac{\partial \mathbf{H}_y}{\partial t} = \frac{\partial \mathbf{E}_z}{\partial x}-\frac{\partial \mathbf{E}_x}{\partial z} \tag{7}$$

$$\mu\frac{\partial \mathbf{H}_z}{\partial t} = \frac{\partial \mathbf{E}_x}{\partial y}-\frac{\partial \mathbf{E}_y}{\partial x}. \tag{8}$$

Assuming a plane-polarized radiation source, Maxwell's equations decouple into one of two polarization states: transverse electric mode (*TE*) and transverse magnetic mode (*TM*). For two-dimensional problems, assumed uniform and infinite in the *z*-direction, the *TE* equations reduce to

$$\varepsilon\frac{\partial \mathbf{E}_z}{\partial t} = \frac{\partial \mathbf{H}_y}{\partial x}-\frac{\partial \mathbf{H}_x}{\partial y}-\sigma_e\mathbf{E}_z \tag{9}$$

$$\mu\frac{\partial \mathbf{H}_x}{\partial t} = -\frac{\partial \mathbf{E}_z}{\partial y} \tag{10}$$

$$\mu\frac{\partial \mathbf{H}_y}{\partial t} = \frac{\partial \mathbf{E}_z}{\partial x} \tag{11}$$

and the TM equations are expressed as

$$\mu\frac{\partial \mathbf{H}_z}{\partial t} = \frac{\partial \mathbf{E}_x}{\partial y}-\frac{\partial \mathbf{E}_y}{\partial x} \tag{12}$$

$$\varepsilon \frac{\partial \mathbf{E}_x}{\partial t} = \frac{\partial \mathbf{H}_z}{\partial x} \tag{13}$$

$$\varepsilon \frac{\partial \mathbf{E}_y}{\partial t} = -\frac{\partial \mathbf{H}_z}{\partial x} - \sigma_e \mathbf{E}_y. \tag{14}$$

The *TM* equations contain only the electric field in the x–y plane along with the induced magnetic field and the *TE* equations contain only the magnetic field in the x–y plane along with the induced electric field. In this study we consider only *TE* polarization, although *TM* polarization could just as easily be simulated.

The FDTD formulation is obtained by approximating temporal and spatial derivatives using central differencing (second-order accurate). The electric and magnetic fields are interweaved both spatially and temporally, resulting in a leapfrog scheme [25]. The electric field vector components are offset one half cell in the direction of their corresponding components, while the magnetic field vector components are offset one half cell in each direction orthogonal to their corresponding components. The **E** and **H**-fields are evaluated at alternate half time steps. For *TE* mode, the electric and magnetic field components are obtained as

$$\begin{aligned} E_z^n(i,j) = {} & \frac{1 - \dfrac{\sigma_e(i,j)\Delta t}{2\varepsilon(i,j)}}{1 + \dfrac{\sigma_e(i,j)\Delta t}{2\varepsilon(i,j)}} E_z^{n-1}(i,j) \\ & + \frac{\Delta t}{\varepsilon(i,j)} \frac{1}{1 + \dfrac{\sigma_e(i,j)}{2\varepsilon(i,j)}} \\ & \cdot \left\{ \frac{H_y^{n-1/2}(i+1/2,j) - H_y^{n-1/2}(i-1/2,j)}{\Delta x} \right. \\ & \left. + \frac{H_x^{n-1/2}(i,j-1/2) - H_x^{n-1/2}(i,j+1/2)}{\Delta y} \right\} \end{aligned} \tag{15}$$

$$\begin{aligned} H_x^{n+1/2}(i,j+1/2) = {} & H_x^{n-1/2}(i,j+1/2) \\ & + \frac{\Delta t}{\mu(i,j+1/2)} \left\{ \frac{E_z^n(i,j) - E_z^n(i,j+1)}{\Delta y} \right\} \end{aligned} \tag{16}$$

$$\begin{aligned} H_y^{n+1/2}(i+1/2,j) = {} & H_y^{n-1/2}(i+1/2,j) \\ & + \frac{\Delta t}{\mu(i+1/2,j)} \left\{ \frac{E_z^n(i+1,j) - E_z^n(i,j)}{\Delta x} \right\}. \end{aligned} \tag{17}$$

Similar equations can be obtained for the *TM* mode through use of duality. Interfaces between media can be easily handled, although they must be placed at integer nodes. Unique electromagnetic properties can be assigned to each unit cell in the lattice, enabling straightforward computation of inhomogeneous problems; an important ability when properties are temperature dependent. In addition, since each unit cell has all six electromagnetic components, anisotropic materials can also be modeled by specifying unique properties at sub-cell nodes. Although schemes have been developed to handle curved surfaces, i.e. non-rectangular geometries, as long as the grid size is small compared with an object's dimensions, rectangular grids will be sufficient [18].

The choice of spatial and temporal resolution is motivated by reasons of stability and accuracy. To insure stability of the time-stepping algorithm, Δt must be chosen to satisfy the Courant stability condition

$$\Delta t \leqslant \frac{1}{c_{\max}\sqrt{\dfrac{1}{\Delta x^2} + \dfrac{1}{\Delta y^2} + \dfrac{1}{\Delta z^2}}}, \tag{18}$$

where $c_{\max}$ is the maximum electromagnetic wave phase velocity within the media modeled. For the two-dimensional case, the corresponding numerical stability expression can be obtained by setting $\Delta z \to \infty$. Clearly, the spatial resolution must insure adequate sampling to avoid aliasing of the smallest wavelength encountered. Generally, to achieve accurate solutions, the spatial resolution should closely approach the situation where an integer number of cells span a wavelength. In a cavity with a highly conductive enclosure containing a sample, the wavelength within the sample changes to reflect the jump in refractive index from the surrounding air. Consequently, determination of spatial resolution should consider cavity and sample configuration as well as electric properties. In addition, numerical dispersion (a variation in numerical wave phase velocity with wavelength and propagation direction) arises from lattice discretization, leading to such non-physical results as artificial anisotropy and pseudo-refraction. The spatial mesh must be small enough to reduce numerical dispersion to an acceptable level.

3. ELECTRIC FIELD DISTRIBUTIONS IN A TWO-DIMENSIONAL WAVEGUIDE-CAVITY

To assess the variation of electric fields in a typical microwave processing cavity, we examine a simple two-dimensional multi-mode cavity operating in the TE_{33} mode. A short square waveguide, centered at one of the faces, is used to deliver a microwave planar source sinusoidally distributed in space and time with a peak amplitude of 1000 V m^{-1}. The size of the waveguide was chosen to be $\sqrt{2}/2\lambda_0$ (8.67 × 8.67 cm), where $\lambda_0 = c_0/f$ is the corresponding wavelength in free space for a frequency of $f = 2.45$ GHz. The cavity size is set to $3/2\sqrt{2}\lambda_0$ (26 × 26 cm). Figure 1 shows a schematic of the waveguide and cavity, and includes a square specimen of dimension 8.67 × 8.67 cm at the cavity center. The walls of the cavity and waveguide are modeled as nearly perfect electrical conductors.

The computational domain is conservatively set such that the spatial resolution of each cell is

$\Delta x = \Delta y = \sqrt{2}/40\lambda_0$, thus providing 60×60 cells in the cavity and 20×20 cells in the waveguide. The temporal resolution is determined by $\Delta t = \Delta x/(\sqrt{2}c_0)$, which satisfies the stability criterion set in equation (18). The excitation source is modeled as time harmonic, thus the root-mean-square value can be computed over a half cycle period at each spatial point.

Figure 2a–c displays the E_{rms} field within an empty cavity and waveguide for three different operating frequencies after 10 000 time steps. Figure 2a shows the resulting square modal patterns corresponding to the 2.45 GHz resonant frequency. In this case the cavity is highly resonant and supports nearly perfect standing waves. Figure 2b,c illustrates the non-resonant characteristics achieved with source frequencies of $\pm 10\%$ of the resonant frequency. By introducing waves differing from the resonant frequency, there is a continuous change in phase of wavefronts arriving at any given grid point (no consistent constructive interference) and hence the amplitudes of the E_{rms} fields are modulated over time. Consequently, the E_{rms} values are lower and more uniform than in the resonant case.

Power absorption in an electromagnetically heated material is often quantified with respect to the skin depth, the distance in which the electric field amplitude falls to e^{-1} of its value at the material surface. In terms of optical parameters, the skin depth is defined as [26]

$$\delta = \frac{n\lambda}{k2\pi}, \tag{19}$$

where n and k are the real and imaginary indices of refraction. In terms of electrical properties, the skin depth can be expressed as [24]

$$\delta = \frac{1}{\omega\sqrt{\mu\varepsilon}(\frac{1}{2}\sqrt{1+(\sigma/\omega\varepsilon)^2}-1)^{1/2}}. \tag{20}$$

While informative for understanding the difference in material properties, skin depth does not adequately address the influence of cavity and sample size and geometry, which can be uncovered via detailed simulation.

Figure 3a–d displays E_{rms} values with 8.67×8.67 cm specimen in the cavity at 2.45 GHz. The electrical conductivity (S m^{-1}) (Siemen m^{-1}) and the relative dielectric constant for Fig. 3a–d are 0.1 and 2, 0.1 and 4, 0.1 and 8 and 0.33 and 8, respectively. Figure 3a shows that the presence of the specimen can disrupt the E_{rms} pattern in the cavity significantly. Figure 3b displays a symmetric pattern in both x and y direc-

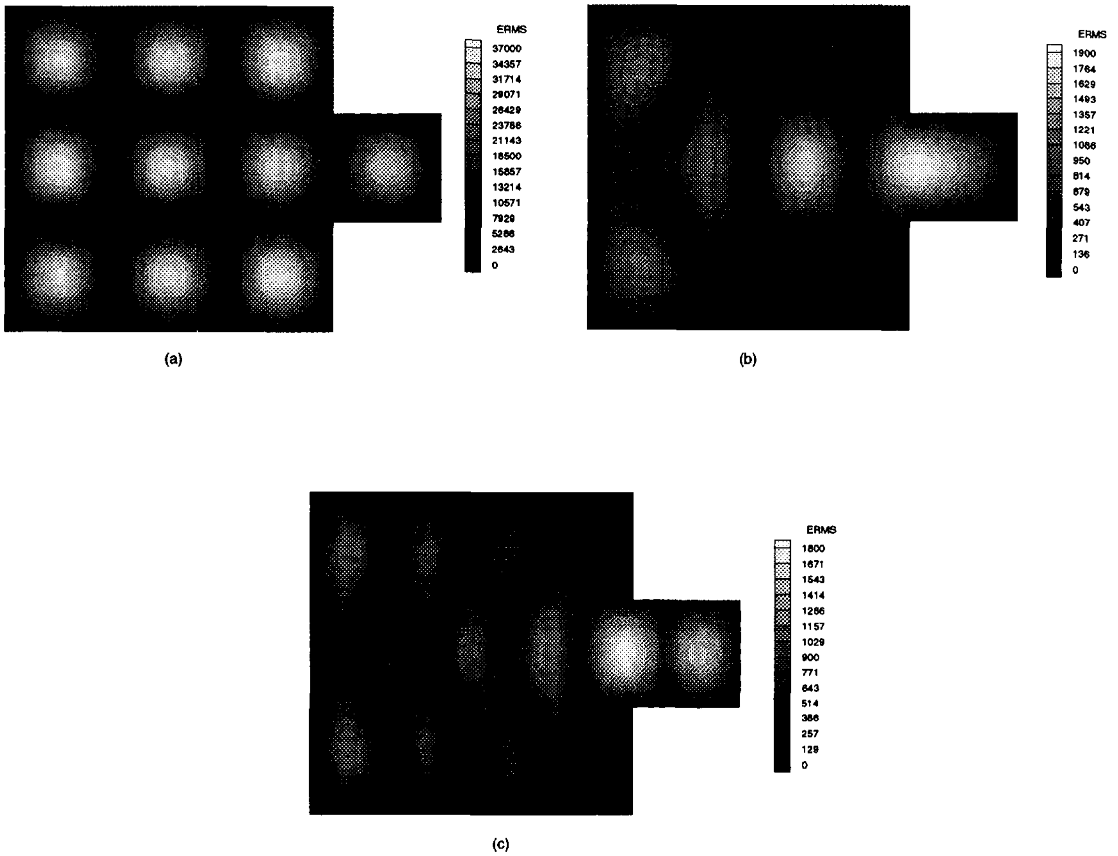

Fig. 2. E_{rms} (V m^{-1}) pattern in an empty cavity at (a) 2.45 GHz, (b) 2.205 GHz (-10%), and (c) 2.695 GHz ($+10\%$).

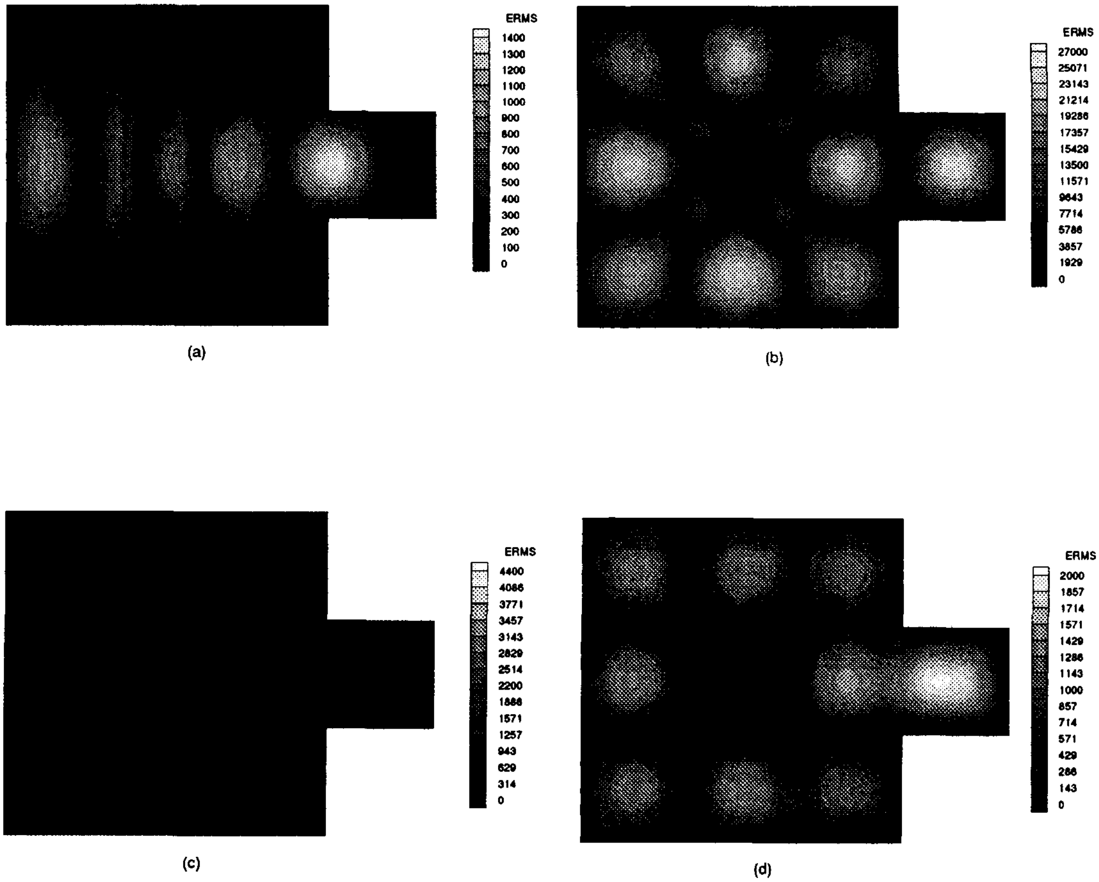

Fig. 3. E_{rms} (V m^{-1}) pattern in an empty cavity at (1) $\varepsilon_r = 2.0$ and $\sigma_e = 0.01$ S m^{-1}, (b) $\varepsilon_r = 4.0$ and $\sigma_e = 0.01$ S m^{-1}, (c) $\varepsilon_r = 8.0$ and $\sigma_e = 0.01$ S m^{-1}, and (d) $\varepsilon_r = 8.0$ and $\sigma_e = 0.33$ S m^{-1}.

tions, a result of phase matching of reflections off the specimen and walls. This pattern depicts a resonant behavior, as exemplified by the high local intensities throughout the cavity. Note that the modal pattern of 3 x 3 squares is still evident. Figure 3c displays nearly symmetric behavior, indicative of patterns in the neighborhood of a resonance. In this instance, the E_{rms} values are much higher than those shown in Fig. 3a, but still significantly less than the resonant condition of Fig. 3b. Comparing Fig. 3c and d shows that increasing σ_e redistributes the fields and further lowers the field values. Identification of very local field variations illustrates the ability of the FDTD approach to detect very local physical changes, significant when heating materials with impurities (such as local voids or small metallic particles) or inhomogeneity due to temperature dependence.

To illustrate the effect of property variation on absorption, Table 1 shows the total electromagnetic power (nondimensionalized with respect to the maximum value simulated) absorbed by the specimen for a range of electrical properties. The total average power absorbed per unit depth can be calculated by summing over each node in the material sample, i.e.

$$Q_{\mathrm{total}} = \Sigma_i \Sigma_j \sigma_e |E_{\mathrm{rms}}|^2 \Delta x \Delta y. \qquad (21)$$

The power absorbed by the sample with a relative dielectric constant, $\varepsilon_r = \varepsilon/\varepsilon_0$, equal to 2.0 exhibited a steady increase as the electrical conductivity was increased. This trend can be attributed to the decrease in the penetration depth of the material. The power absorbed when ε_r equals 4.0 exhibited the opposite behavior with increasing electrical conductivity. In this case the power absorbed by the sample was dominated by a resonant behavior. The sample size and geometry, in conjunction with the index of refraction, determine the relative phase of the wavefronts in the sample and hence the amounts of constructive interference. Resonant behavior is also depicted when ε_r equals 8.0. In this case the resonance is not as strong

Table 1. Dimensionless power absorption in an 8.67 × 8.67 cm^2 sample

	σ_e (S m^{-1})				
ε_r	0.01	0.03	0.1	0.3	1.0
2.0	0.008	0.024	0.050	0.063	0.065
4.0	1.000	0.340	0.152	0.085	0.073
8.0	0.100	0.062	0.047	0.073	0.084
12.0	0.125	0.279	0.249	0.126	0.094

and the power absorbed dips at around $\sigma_e = 0.1$ S m^{-1}. The power absorbed when ε_r equals 12.0 exhibits a maximum near the middle of the electric conductivity range, indicating resonance. These results illustrate that the power absorbed is strongly dependent on whether the system is at or near resonance.

Table 2 displays the dimensionless power absorption for a variety of sample sizes with different dielectric constants (the electrical conductivity is 0.1 S m^{-1}). The underlying trend displayed in Table 2 is a steady increase in power deposition with sample size until a critical dimension is reached, in this case 13×13 cm^2, followed by a steady decrease. This phenomenon is analogous to the concept of cut-off frequency. Simply stated, electromagnetic waves cannot propagate between guiding surfaces separated by less than one-half wavelength. In this case, when the distance between the sample edges and the cavity walls is less than $\lambda_0/2 = 6.13$ cm the waves are strongly attenuated as they attempt to propagate around the sample. Thus, the effective surface area for wave penetration into the sample is reduced and the power deposition decreases accordingly. However, since resonant behavior is achieved for some of the situations encountered, e.g. samples of ε_r equal to 4.0 and 12.0, absorption peaks will occur at sample sizes below cut-off. At sample sizes above cut-off, where there are no resonances, power absorption will decrease with increasing ε_r, since absorption occurs mostly at the front surface (note, the skin depth δ increases with ε_r in this frequency regime).

4. HEAT TRANSPORT

Since our ultimate interest is in the thermal effect microwave energy imparts to materials, accurate computations of spatial and temporal temperature changes are imperative to achieve basic understanding and control of heating processes. This is especially important for materials in which absorption of microwave energy is highly temperature dependent.

The governing energy equation describing the temperature rise in the heated material is the time-dependent heat diffusion equation,

$$\rho C \frac{\partial T}{\partial t} = \nabla \cdot (k \nabla T) + Q_{\mathrm{em}}, \tag{22}$$

where ρ, C and k are the sample density, specific heat and thermal conductivity, respectively. The local electromagnetic heat source Q_{em} is directly dependent upon the local value of the electric field,

$$Q_{\mathrm{em}} = \sigma_e |\mathbf{E}|^2. \tag{23}$$

Heat is lost from the sample via natural convection and radiation. The convective heat flux is computed along the edges of the sample using

$$q_{\mathrm{conv}} = h_f (T_e - T_a), \tag{24}$$

where the subscripts e and a are used to denote sample edge and ambient temperatures, respectively. The radiative heat flux from a surface element i to the cavity walls is computed as

$$q_{\mathrm{rad}_{i-w}} = \sigma \varepsilon (T_i^4 - T_w^4), \tag{25}$$

where ε denotes radiative emissivity (assumed the same on both sample and walls), and σ is the Stefan–Boltzman constant. (In this work, the sample surface does not see itself and the surfaces are diffuse.)

An explicit finite difference method is used to solve the temperature field (the discretization formulation can be found in any elementary heat transfer text, e.g. [27]). The significant aspect pertains to the coupling of the thermal and electromagnetic solvers. Heat source terms are provided at each temperature node, so that the mesh used to solve the thermal problem is identical to that employed for the E-field solution. Since the time scale for electromagnetic transients is much smaller than the thermal response, Q_{em} can be computed in terms of the local root-mean-square value of **E**. An iterative solution procedure is required when electromagnetic properties are temperature dependent. Calculation of the two governing equations on the same time scale is not feasible from a computational standpoint because of scale disparity. Instead, electromagnetic property changes with temperature are monitored as processing proceeds and a criterion is established to determine when an electromagnetic computation is necessary to update the heat source for the thermal computation.

5. SIMULATION OF THERMAL RUNAWAY

To illustrate a difficult microwave heating simulation, a specimen is chosen with highly temperature dependent electromagnetic properties, alumina. Alumina is a widely used ceramic with well-known electromagnetic properties. For simplicity, temperature dependent data for the electrical conductivity and relative dielectric constant of 99.5% alumina [28] at 2.45 GHz are fitted to a third-order polynomial, plotted vs temperature in Fig. 4. Thermal properties are considered constant with temperature: thermal conductivity $k = 1.381$ W m^{-1} °C^{-1}, specific heat $C = 753.1$ kJ kg^{-1} °C^{-1}, density $\rho = 3820$ kg m^{-3},

Table 2. Dimensionless power absorption for different sample sizes with $\sigma_e = 0.1$ S m^{-1}

Sample dimension (cm)	ε_r			
	2.0	4.0	8.0	12.0
5.20 × 5.20	0.122	0.062	0.156	0.086
6.93 × 6.93	0.128	0.240	0.107	0.198
8.67 × 8.67	0.201	0.611	0.190	1.000
10.40 × 10.40	0.305	0.470	0.285	0.311
13.00 × 13.00	0.380	0.421	0.520	0.394
15.60 × 15.60	0.266	0.193	0.156	0.104
18.20 × 18.20	0.170	0.127	0.086	0.070

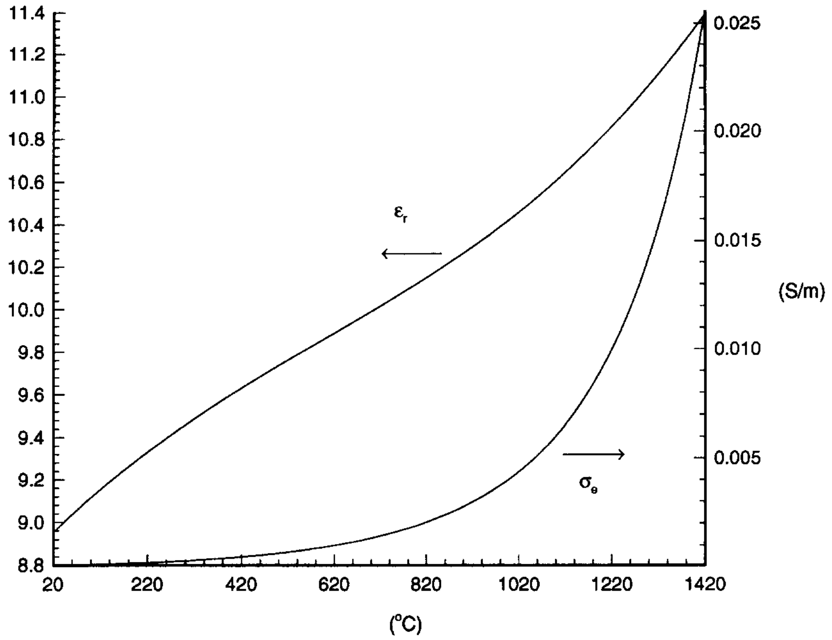

Fig. 4. Temperature dependence of dielectric properties for 99.5% alumina.

emissivity $\varepsilon = 0.6$, and heat transfer coefficient $h_f = 5$ W m^{-2} °C^{-1}, representing free convection. The cavity walls are maintained at a constant temperature and have an emissivity of 0.6. Initially, the cavity and sample are at a uniform temperature of 20°C. Cavity and waveguide dimensions and mesh resolution are identical to the previous simulations, and the sample is square, 8.67 × 8.67 cm^2. In this simulation we choose a fixed frequency of 2.45 GHz, widely used for domestic and some industrial applications.

The numerical procedure is to first compute a local heat source by running an electromagnetic simulation with uniform properties, determined from room temperature data. The electromagnetic simulation is performed until a sufficient period is reached in which a representative average rms of the E-field at each spatial point is obtained, typically 40 000 time steps. The power deposition at each point is then computed and used to solve the time-dependent temperature field. As the thermal solver proceeds, the electrical conductivity is monitored. Once the local value of σ_e changes 10% at any location from its value at the previous iteration, the electromagnetic field is then recomputed using updated dielectric properties. (A number of iteration criteria were tested. The value of 10% was determined to provide consistent temperature profiles.)

Electric fields in the cavity/waveguide, including the sample, after the first and last iteration are shown in Fig. 5a,b, respectively. The first iteration, Fig. 5a, is performed with constant properties throughout the specimen. The field distribution within the sample shows two well-defined peaks near the upper and lower front corners (closest to the waveguide). Peaks of approximately half this magnitude can be seen near

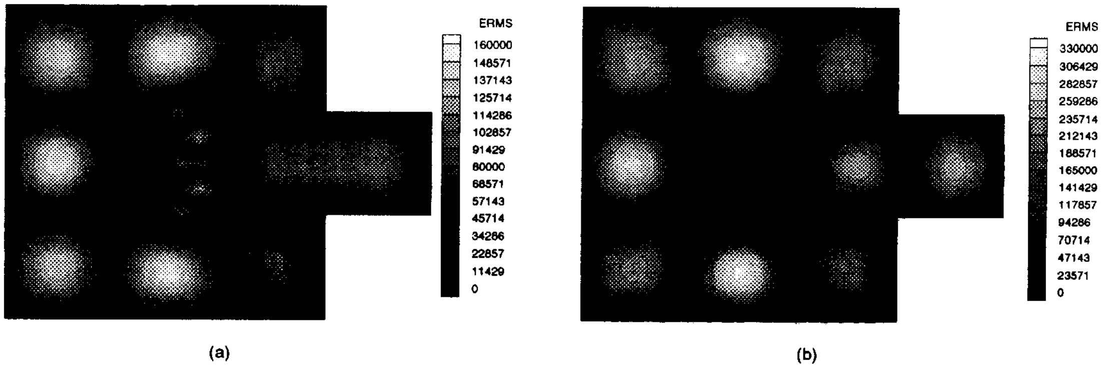

(a) (b)

Fig. 5. E_{rms} (V m^{-1}) pattern in a cavity with alumina specimen at (a) 7 min and (b) 74 min.

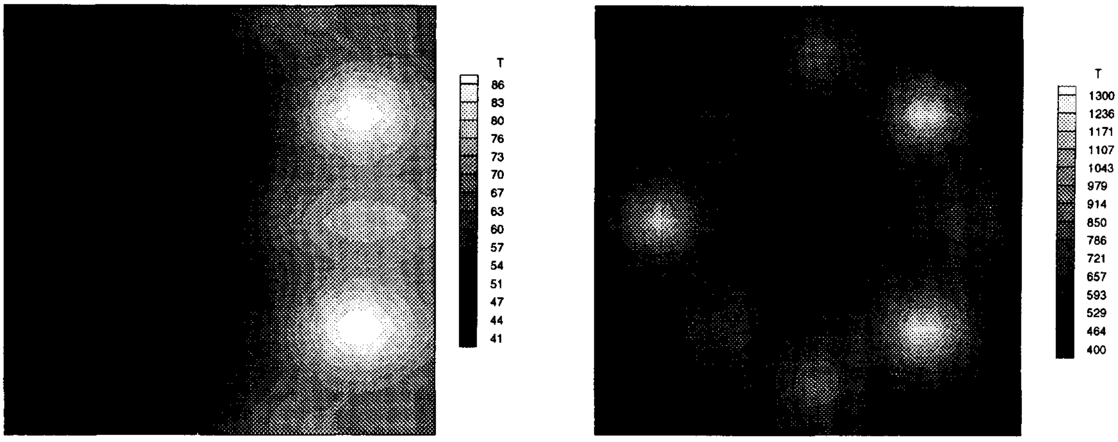

(a) (b)

Fig. 6. Temperature distribution in alumina sample at (a) 7 min and (b) 74 min.

the back corners and near the center of the front and rear edges. Thus, the energy deposition at the hot spots in the front are approximately four times that found at the hot spots in the rear (since energy deposition is related to $\mathbb{E}^2$). The temperature distribution at the end of the first iteration, i.e. before another electromagnetic update, is shown in Fig. 6a, which corresponds to a heating period of 7 min. Note that the presence of hot spots, seen at the specimen front face, is consistent with the electric field pattern shown in Fig. 5a. Diffusion from the hot spots heats the entire front section, whereas the back section, with much lower energy deposition, remains relatively cool. Steep temperature gradients between the front and back sections are shown along the entire length down the midplane of the sample.

Figures 5b and 6b show the electric field and temperature distribution at the last iteration, after 74 min of processing. At this stage σ_e has changed significantly throughout the specimen. Comparison of the initial electric and thermal fields shown in Figs. 5a and 6a, respectively, with the fields at the last iteration (Figs. 5b and 6b) displays the significant changes brought about by the variation in σ_e with temperature. As the hot spots in the front of the sample increase in temperature the electric fields are redistributed more symmetrically throughout the sample, indicative of a cavity which has approached a resonant mode. This is an interesting observation since the results displayed in Fig. 5a display nonresonant behavior. Although thermal diffusion from the sample front to the rear section occurs, it is the redistribution of microwave energy that most strongly effects the thermal field in the sample, as evidenced by the locus of eight electric and thermal peaks.

As the sample temperature reaches higher values, slight temperature differences can exhibit large variations in σ_e, resulting in an exponential local temperature rise, or thermal runaway. In this situation, thermal diffusion and heat loss cannot keep pace with energy deposition at the sample hot spots. This is evidenced in Fig. 7, which shows the rise over time for the maximum, minimum, average and center temperatures. Notice that there is no definitive level at which local temperatures begin to take-off, but rather the sharp bend in the curve covers a range of approximately 10°C. This phenomenon is due to the fact that thermal diffusion slows down the temperature rise at the local hot spots, while increasing the temperature throughout the sample.

6. CONCLUSIONS

A detailed numerical model is presented for solving Maxwell's equations in a microwave cavity containing a specimen. The model can be used to determine modal patterns in the cavity, detecting both resonant and non-resonant conditions. Simulations are performed to illustrate the influence specimen size and electrical properties have on microwave absorption and electric field patterns. The energy deposition in the sample can be computed from the electromagnetic simulations, allowing determination of the evolution of the thermal profile.

To illustrate the power of the numerical technique, a strongly coupled electromagnetic-thermal problem is simulated, i.e. thermal runaway in a ceramic material. This phenomenon, caused by an exponential increase in electrical conductivity with temperature, presents a major challenge for microwave designers and processing engineers since poor product quality and sample cracking are often exhibited if temperature levels and distributions cannot be controlled. The simulation assists our understanding of how materials are heated and how temperature dependent dielectric properties influence electric field and temperature distributions. In future work we will examine methods to avoid thermal runaway, or control it by using variable input power control and variable frequency processing.

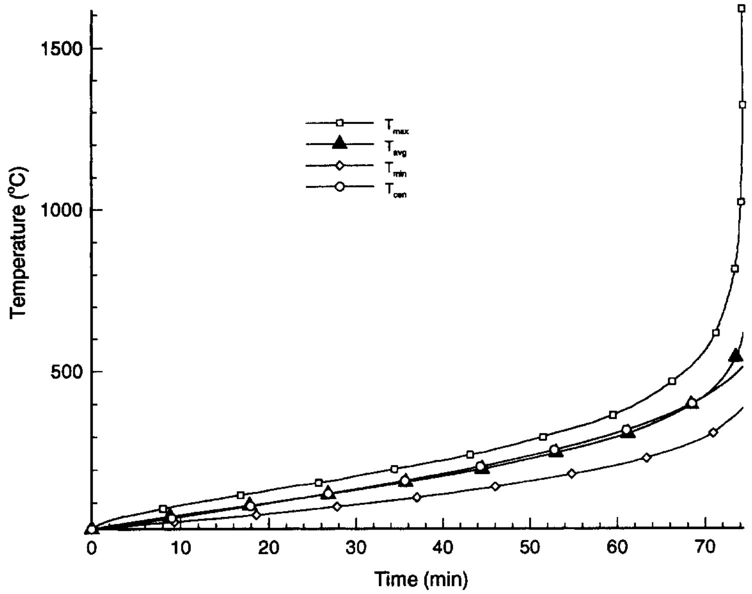

Fig. 7. Temperature rise over time in alumina specimen.

REFERENCES

1. W. S. Sutton, Microwave processing of ceramic materials, *Ceramic Bull.* **68,** 376–386 (1989).
2. W. S. Sutton, Microwave processing of ceramics—an overview. In *Microwave Processing of Materials III* (Edited by R. L. Beatty, W. S. Sutton and M. F. Iskander), Vol. 269, pp. 3–20. Materials Research Society, Pittsburgh, PA (1992).
3. D. A. Lewis, Microwave processing of polymers—an overview. In *Microwave Processing of Materials III* (Edited by R. L. Beatty, W. S. Sutton and M. F. Iskander), Vol. 269, pp. 21–31. Materials Research Society, Pittsburg, PA (1992).
4. W. Jie and Y. Jiankang, Behaviour of coal pyrolysis desulfurization with microwave energy, *Fuel* **73,** 155–159 (1994).
5. C. E. George, G. R. Lightsey, I. Jun and J. Fan, Soil decontamination via microwave and radio frequency co-volatization, *Environ. Prog.* **11,** 216–219 (1992).
6. E. Moore, D. Clark and R. Hutcheon, Polymethyl methacrylate binder removal from an alumina compact: Microwave versus conventional heating. In *Microwave Processing of Materials III* (Edited by R. L. Beatty, W. S. Sutton and M. F. Iskander), Vol. 269, pp. 341–346. Materials Research Society, Pittsburgh, PA (1992).
7. S. J. Oda, Dielectric processing of hazardous materials—present and future opportunities. In *Microwave Processing of Materials III* (Edited by R. L. Beatty, W. S. Sutton and M. F. Iskander), Vol. 269, pp. 453–464. Materials Research Society, Pittsburgh, PA (1992).
8. M. Arai, J. G. Binner, G. E. Carr and T. E. Cross, High temperature dielectric measurements on ceramics. In *Microwave Processing of Materials III* (Edited by R. L. Beatty, W. S. Sutton and M. F. Iskander), Vol. 269, pp. 611–616. Materials Research Society, Pittsburgh, PA (1992).
9. D. L. Johnson, D. J. Skamser and M. S.Spotz, Temperature gradients in microwave processing: Boon and bane. In *Ceramic Transactions: Microwave Theory and Applications in Materials Processing II* (Edited by D. E. Clark, W. R. Tinga and J. R. Laia), Vol. 36, pp. 133–145. The American Ceramic Society, Westerville, OH (1993).
10. W. Xi and W. R. Tinga, Microwave heating and characterization of machinable ceramics. In *Microwave Processing of Materials III* (Edited by R. L. Beatty, W. S. Sutton and M. F. Iskander), Vol. 269, pp. 569–577. Materials Research Society, Pittsburgh, PA (1992).
11. J. A. Batt, R. Ruckus and M. Gilden, General purpose high temperature microwave measurement of electromagnetic properties. In *Microwave Processing of Materials III* (Edited by R. L. Beatty, W. S. Sutton and M. F. Iskander), Vol. 269, pp. 553–559. Materials Research Society, Pittsburgh, PA (1992).
12. K. G. Ayappa, H. T. Davis, E. A. Davis and J. Gordon, Two-dimensional finite element analysis of microwave heating, *AIChE J.* **38,** 1577–1592 (1992).
13. G. Roussy, A. Bennani and J. M. Thiebaut, Temperature runaway of microwave irradiated materials, *J. Appl. Phys.* **62,** 1167–1170 (1987).
14. Y. L. Tian, J. H. Feng, L. C. Sun and C. J. Tu, Computer modeling of two dimensional temperature distributions in microwave heated ceramics. In *Microwave Processing of Materials III* (Edited by R. L. Beatty, W. S. Sutton and M. F. Iskander), Vol. 269, pp. 41–46. Materials Research Society, Pittsburgh, PA (1992).
15. G. A. Beale and F. J. Arteaga, Automatic control to prevent thermal runaway during microwave joining of ceramics. In *Microwave Processing of Materials III* (Edited by R. L. Beatty, W. S. Sutton and M. F. Iskander), Vol. 269, pp. 265–270. Materials Research Society, Pittsburgh, PA (1992).
16. M. N. O. Sadiku, *Numerical Techniques in Electromagnetics.* CRC Press, Boca Raton, FL (1992).
17. K. S. Kunz and J. Luebbers, *The Finite Difference Time Domain Method for Electromagnetics.* CRC Press, Boca Raton, FL (1993).
18. A. Taflove and K. R. Umashankar, The finite-difference time domain method for numerical modeling of electromagnetic wave interactions with arbitrary structures. In *Finite Element and Finite Difference Methods in Electromagnetic Scattering* (Edited by M. Morgan), pp. 287–373. Elsevier, New York (1990).
19. E. K. Miller, Time-domain modeling in electromagnetics, *J. Electromagnet. Waves Applic.* **8,** 1125–1172 (1994).
20. M. F. Iskander, Computer modeling and numerical techniques for quantifying microwave interactions with

materials. In *Microwave Processing of Materials II* (Edited by W. B. Synder, W. S. Sutton, M. F. Iskander and D. L. Johnson), Vol. 189, pp. 149–171. Materials Research Society, Pittsburgh, PA (1992).

21. M. F. Iskander, O. Andrade, H. Kimrey, R. Smith and S. Lamoreaux, Computational techniques in modeling and quantifying microwave interactions with materials. In *Ceramic Transactions: Microwave Theory and Applications in Materials Processing II* (Edited by D. E. Clark, F. D. Gac and W. H. Sutton), Vol. 21, pp. 141–158. The American Ceramic Society, Westerville, OH (1993).
22. R. L. Smith, M. F. Iskander, O. Andrade and H. Kimrey, Finite-difference time-domain (fdtd) simulation of microwave sintering in multimode cavities. In *Microwave Processing of Materials III* (Edited by R. L. Beatty, W. S. Sutton and M. F. Iskander), Vol. 269, pp. 47–52. Materials Research Society, Pittsburg, PA (1992).
23. B. Chapman, M. F. Iskander, R. L. Smith and O. M. Andrade, Simulation of sintering experiments in single-mode cavities. In *Microwave Processing of Materials III* (Edited by R. L. Beatty, W. S. Sutton and M. F. Iskander), Vol. 269, pp. 53–59. Materials Research Society, Pittsburgh, PA (1992).
24. C. A. Balanis, *Advanced Engineering Electromagnetics*. Wiley, New York (1989).
25. K. S. Yee, Numerical solution of initial boundary value problems involving Maxwell's equations in isotropic media, *IEEE Trans. Antennas Propagation* **AP-14,** 302–307 (1966).
26. J. R. Reitz, F. J. Milford and R. W. Christy, *Foundations of Electromagnetic Theory*. Addison Wesley, Reading, MA (1980).
27. F. P. Incropera and D. P. Dewitt, *Fundamentals of Heat and Mass Transfer*. Wiley, New York (1985).
28. S. Al-Assafi and D. E. Clark, Microwave joining of ceramics: A study on joining alumina both directly and with alumina gel. In *Microwave Processing of Materials III* (Edited by R. L. Beatty, W. S. Sutton and M. F. Iskander), Vol. 269, pp. 335–340. Materials Research Society, Pittsburgh, PA (1992).